3D-simulation of sound propagation through the wake of a wind turbine: impact of the diurnal variability

Dietrich Heimann, Antonia Englberger

Institut für Physik der Atmosphäre

Deutsches Zentrum für Luft- und Raumfahrt e.V.

Weßling-Oberpfaffenhofen, Germany

ABSTRACT

Coupled three-dimensional numerical flow and sound propagation simulations were performed for four different times of a diurnal cycle in the area downwind of a wind energy converter with a hub height of 100 m and a rotor radius of 50 m. The sound propagation from the turbine is subject to vertical and lateral refraction in the wind speed deficit of the wake. The latter is influenced by the varying static stability and turbulence condition of the atmospheric boundary layer. The sound level near the ground is significantly increased by the atmospheric and wake-induced refraction for distances larger than eight times the rotor diameter. This increase is strongest in the morning and evening hours when it locally amounts up to 18 dB. Three-dimensional propagation effects are evident and cannot be neglected. A significant sound-level variation during the turbine revolution is simulated for the evening situation in the far field.

KEYWORDS:

wind turbine, wake flow, sound propagation, diurnal cycle, numerical simulation

Corresponding author:

Dr. Dietrich Heimann

Deutsches Zentrum für Luft- und Raumfahrt e.V.

Institut für Physik der Atmosphäre

Oberpfaffenhofen

82234 Weßling

Germany

eMail: dietrich.heimann@dlr.de (D. Heimann)

1. Introduction

Wind energy converters emit sound which is mostly produced by the interaction between the rotating blades and the turbulent air that impinges on and flows around the blades (aerodynamic noise; e.g. Kim et al. [22]). Further sound is produced by the generator and diverse auxiliary drives to control yaw and pitch. The problems of wind turbine noise in the environment (emission, propagation, impact on human health) are summarized by Rogers et al. [32] or Tabassum-Abbasi et al. [36]. The perception of wind turbine noise by people (annoyance) is addressed for instance by Pedersen et al. [29]. The local impact of noise depends not only on the sound emission at the turbine, but also on the propagation of the sound waves through the atmosphere. Both emission and propagation are determined by the inflow condition (wind profile, temperature stratification, and turbulence) and the operating condition of the turbine. The propagation is additionally influenced by the specific wake due to the moving rotor blades, e.g. Vermeer et al. [39], and the underlying ground. The wake structure was investigated by Lidar measurements, e.g. Bingöl et al. [3], Trujillo et al. [38] and Käsler et al. [21], and numerical simulations, e.g. Wussow et al. [40], Jimenez et al. [20], Troldborg et al. [37], Gross [13], Sørensen et al. [35], or Gebraad et al. [12].

Only in recent years publications appeared that consider the influence of the wake flow in predicting the far-field sound impact by wind converters. Heimann et al. [17] used a three-dimensional ray-based model which was coupled to two different Reynolds-averaged numerical flow models. They found that the sound impact is very sensitive to details in the meteorological fields. Lee et al. [24] used a 2-dimensional diagnostic wave-based propagation model with axisymmetric approximation and successfully compared the results with measurements. Barlas et al. [1] studied the influence of the wake on the sound impact above plane ground. They used a two-dimensional wave-based sound propagation model that was coupled with a large-eddy simulation (LES) of the air flow. It turned out that during stable stratification the sound level can be strongly underestimated if the turbine wake is not considered. A consistent modelling procedure of the wind turbine noise problem is proposed by Barlas et al. [2] who coupled an aerodynamic emission model for wind turbine noise with a LES flow model to simulate the wake flow with an actuator line approximation of the wind turbine blades, and an acoustic propagation model based on the parabolic equation (PE). A similar approach is followed by Cotté [5]. Since the PE models of [2] and [5] are only two-dimensional they are applied in vertical slices that are connecting emission points near the rotating blade tips with diverse ground-based receiver point around the turbine.

A shortcoming of two-dimensional sound propagation modelling in a vertical plane is the neglect of horizontal refraction due to horizontal gradients of wind and/or temperature. In an undisturbed atmosphere vertical gradients of both wind and temperature prevail and therefore the influence of horizontal refraction is negligible. However, once obstacles such as hills, buildings, trees or wind turbines retard or deflect the air flow, horizontal gradients become important. In the case of the wake flow downstream of wind energy converters vertical and horizontal gradients in the wind field are of the same magnitude (e.g. Fig. 7 in Trujillo et al. [38]). This implies that refraction of sound waves not only occurs in the upward and downward directions but also in all other directions (horizontal and slant). Sound waves emerging from the blades into the wake flow therefore pass a three-dimensional system of acoustical lenses leading to local focusing and caustics or to defocusing of the sound rays.

The present paper aims at the numerical simulation of sound propagation in the area downwind of a wind turbine in three dimensions. The three-dimensional wind and temperature fields are provided by precursory large-eddy simulations (LES) which consider the resistance of a wind turbine on the air flow. To cover different situations the results of Englberger and Dörnbrack [10] were used. They refer to four selected times of a full diurnal cycle.

The objective of this study is the elucidation of three-dimensional atmospheric sound propagation effects with the help of three-dimensional numerical simulation. The evaluation is limited to the area downwind of a wind turbine which includes the wake of the rotor. Here the influence of the atmospheric structures on the acoustic refraction is in the focus. Therefore the model fully describes refraction due to wind and temperature gradients in three dimensions. An accurate description of the aero-acoustic source as the result of the interaction between the turbulent air stream and the rotating blades ('blade-vortex interaction') is not intended. Nevertheless, the sound emission is realistically prescribed with respect to source position, spectrum and directivity. Moreover, the study does not aim at the time behaviour of sound levels. It rather deals with sound levels averaged over the turbulent time scale. This applies to partial sound levels according to various source positions taken during the revolution of the rotor and the mean sound level over a full rotation.

2. Flow simulation

2.1 Model

The study deals with a 3-blade horizontal-axis wind turbine with a hub height of $z_{hub} = 100$ m above ground and an upwind rotor with a radius of $r = 50$ m or diameter of $D = 100$ m (Englberger and Dörnbrack [9, 10]). The turbine is located in the origin of the coordinate system at $x_0 = y_0 = 0$ on plane ground (Fig. 1).

The multiscale geophysical flow solver EULAG (Smolarkiewicz and Margolin [34]; Prusa et al. [31]; Englberger and Dörnbrack [9]) is applied in the large-eddy simulation (LES) mode to determine the small-scale flow modification by the rotor in the downwind domain. The turbine-induced force is implemented with the blade-element momentum method as a rotating actuator disc (e.g. Branlard [4]; Englberger and Dörnbrack [9]). A turbulent kinetic energy closure (Schmidt and Schumann [33]; Margolin et al. [26]) is applied.

The flow model domain comprises 512 × 512 numerical meshes in the horizontal with a resolution of 5 m (Fig. 1). In the vertical the computational domain extends up to $z = 420$ m with a resolution of 5 m in the lowest 200 m and 10 m above.

As large-scale initial condition a wind is assumed to blow with 10 m/s parallel to the x-axis so that the rotor plane of the turbine lays in the y-z-plane. Further, the wind-turbine simulations are conducted with synchronized turbulent inflow data of a diurnal-cycle driven boundary-layer flow over a homogeneous surface with a constant drag coefficient of 0.1 (Englberger and Dörnbrack [10]).

Four meteorological situations are considered. They represent four different times of a day during a full summer solstice mid-latitude diurnal cycle over grass-covered ground with undisturbed short- and longwave radiation: midnight (00 LT), morning (05 LT), noon (12 LT), and evening (18 LT). LT stands for 'local time'. The situations 00 LT and 12 LT represent a stable and a convective boundary layer, respectively. The situations 05 and 18 LT represent the transition from night to day and vice versa. They are defined to be representative of the time period in which the heat flux changes sign, whereas the convective boundary layer corresponds to the heat flux maximum (here: 140 W/m^2) and the stable boundary to its minimum (here: -10 W/m^2). Further details of the flow simulations, the implementation of the diurnal cycle, and the simulation results are fully described in [9].

For the subsequent acoustical simulations average wind ($\overline{u}$, $\overline{v}$, $\overline{w}$) and temperature ($\overline{T}$) are stored as three dimensional fields for each of the four situations (00, 05, 12, and 18 LT). $\overline{u}$, $\overline{v}$, and $\overline{w}$ are the average wind components in x, y, and z-direction, respectively. $\overline{u}$, $\overline{v}$, $\overline{w}$, and $\overline{T}$ are averaged over 50 minutes, i.e. the full large-eddy simulation time after a 10-min initial spin-up time. In addition to wind and temperature the three-dimensional distribution of the turbulent kinetic energy ($\overline{E}$) is provided. The water vapour concentration (humidity) is not modelled.

2.2 Results

Fig. 2 shows the vertical profiles, for each of the four simulations, of the 50-min average sound speed

$$\overline{c} = \sqrt{\frac{c_p}{c_v} R_d \overline{T}} \quad (1)$$

in the undisturbed upwind domain of the wind turbine. The average sound speed $\overline{c}$ is determined from the simulated average temperature $\overline{T}$ where c_p and c_v are the specific heat capacities of air at constant pressure and volume, respectively, and R_d is the gas constant of dry air. At time 12 LT the sound speed decreases with height as the temperature lapse rate is superadiabatic ($\partial\overline{T}/\partial z < -g/c_p$ with the gravity acceleration g) near the ground and represents a convective boundary layer. Six hours later in the evening at 18 LT the boundary layer has further warmed, but the near-ground superadiabatic gradient has disappeared so that the sound speed decreases uniformly with height and the boundary layer is neutrally stratified. Again six hours later at midnight (00 LT) a strong ground-based inversion layer has formed. Now the boundary layer is stably stratified and the sound speed increases with height up to $z \approx 100$ m. Above this level the sound speed remains unchanged with a negative vertical gradient. In the morning at 05 LT the inversion layer has become slightly deeper and now reaches up to $z \approx 130$ m. The very strong gradient near the ground is replaced by a moderate increase with height. The mean vertical sound-speed gradient in the layer $0 \leq z \leq z_{\mathrm{hub}}$ amounts to $+0.037\ \mathrm{s}^{-1}$ (00 LT), $+0.022\ \mathrm{s}^{-1}$ (05 LT), $-0.014\ \mathrm{s}^{-1}$ (12 LT), and $-0.007\ \mathrm{s}^{-1}$ (18 LT).

The corresponding vertical profiles of the wind components $\overline{u}$ and $\overline{v}$ are shown in Fig. 3 on both sides (upwind and downwind) of the wind turbine. At 12 and 18 LT the $\overline{u}$-profiles are similar on the upwind side. Near the ground the vertical wind speed gradient is rather strong and the prescribed large-scale wind speed of 10 m/s is approached already below the rotor plane. In the downwind domain (200 m behind the turbine) the wind is decelerated in the rotor layer as the wake effect. The wind deficit increases from 12 LT to 18 LT. Below the rotor plane a slight increase of the wind speed is simulated. At 00 LT, after the stabilization of the boundary layer, the inflow wind speed has decreased in the lowest 50 m and slightly increased above $z \approx 80$ m. Five hours later at 05 LT a weak low-level jet (LLJ) has formed as a consequence of the geostrophic-antitriptic imbalance. The wind speed maximum of the LLJ has established at $z \approx 90$ m, i.e. a few meters below the height of the wind turbine hub. In the downwind domain the nightly wind speed minimum in the wake of the rotor is even stronger than in the evening and the vertical gradients at the lower and upper limit of the wake have become rather strong. The $\overline{v}$-profiles reflect the Ekman turning of the wind direction in the boundary layer. The turning is rather weak during unstable and neutral stratification at 12 and 18 LT. It is especially pronounced at 00 and 05 LT in the stable inversion layer. The Ekman-turning implies an asymmetry of the wind field with respect to the *y*-axis.

The simulated wake structure in the downwind domain of the wind turbine is presented in Fig. 4 for the four situations of the diurnal cycle. The figure shows vertical cross-sections through *y*=0 of the effective sound speed $\overline{c}_{\mathrm{eff,x}} = \overline{c} + \overline{u}$ for downstream sound propagation. Gradients of the effective sound speed cause refraction of sound waves, i.e. sound rays are diverted towards the region with smaller values of $\overline{c}_{\mathrm{eff,x}}$. The wind speed reduction in the wake of the turbine is particularly sharp and elongated during the stable stratification of the midnight (00 LT) and morning (05 LT) situation. Under convective conditions at 12 LT the speed deficit only extends a few hundred meters because of high turbulence and corresponding mixing. At 18 LT, when the boundary layer is almost neutrally stratified, the wake is moderate. The different lengths of the wake in stable and unstable conditions agree with other studies (e.g. Gross [13]; Barlas et al. [1]).

The three-dimensional structure of the wake is illustrated in Fig. 5 for the situation 00 LT. The figure shows the spanwise gradient of the effective speed of sound $\bar{c}_{\mathrm{eff,x}}$ for propagation in *x*-direction 400 m downstream of the wind converter. Near the surface this gradient causes downward refraction as it is usual in downwind propagation. In the wake, however, the streamwise propagating sound waves are refracted towards the core of the wake velocity deficit. The maximum magnitude of refraction is independent of the direction of refraction, i.e. lateral and vertical refractions are equally important in the wake of the wind turbine. The asymmetry of the gradient follows from the Ekman-turning below *z* = 120 m (cf. Fig. 3).

3. Sound propagation simulation

3.1 Description of the model

In this study a three-dimensional ray-based sound particle model is used (Heimann and Gross [16]). This Lagrangian type of model is much less expensive than a 3-dimensional time-domain Euler model, for instance. Therefore, it can be applied to a large domain. In [16] the model was compared with analytical results and published benchmark results of a fast-field-program (FFP) model. The model was previously applied to wind turbine noise by Heimann et al. [17].

In the model a large number of so-called sound particles are released at the position of one or several source points from where they propagate into the surrounding airspace. Each particle carries a certain amount of sound energy depending on the strength of the source. The specific sound energy of a particle also depends on its initial direction to account for the source directivity. The particles travel with the speed of sound relative to the moving air along rays which can be curved according to the local gradients of the sound and wind speed (refraction). The ray coordinates are calculated by a numerical time integration of the following equations which determine the position and the direction of travel of the particles (Pierce [30]; Chapter 8):

$$\frac{dx_i}{dt} = (\bar{u} + u') + \bar{c}\, n_{x,i} \tag{2}$$

$$\frac{dy_i}{dt} = (\bar{v} + v') + \bar{c}\, n_{y,i} \tag{3}$$

$$\frac{dz_i}{dt} = (\bar{w} + w') + \bar{c}\, n_{z,i} \tag{4}$$

$$\frac{dn_{x,i}}{dt} = -\frac{\partial \bar{c}}{\partial x} - \left(\frac{\partial(\bar{u} + u')}{\partial x} + \frac{\partial(\bar{v} + v')}{\partial x} + \frac{\partial(\bar{w} + w')}{\partial x} \right) \tag{5}$$

$$\frac{dn_{y,i}}{dt} = -\frac{\partial \bar{c}}{\partial y} - \left(\frac{\partial(\bar{u} + u')}{\partial y} + \frac{\partial(\bar{v} + v')}{\partial y} + \frac{\partial(\bar{w} + w')}{\partial y} \right) \tag{6}$$

$$\frac{dn_{z,i}}{dt} = -\frac{\partial \bar{c}}{\partial z} - \left(\frac{\partial(\bar{u} + u')}{\partial z} + \frac{\partial(\bar{v} + v')}{\partial z} + \frac{\partial(\bar{w} + w')}{\partial z} \right) \tag{7}$$

x_i, y_i, z_i are the position coordinates of the *i*-th particle and $n_{x,i}$, $n_{y,i}$, $n_{z,i}$ are the components of the wave vector of the *i*-th particle which is perpendicular to the wave front and determines the direction of the particle movement relative to the air.

The mean wind components $\overline{u}$, $\overline{v}$, $\overline{w}$ and the mean temperature $\overline{\mathrm{T}}$ are taken from the three-dimensional LES model output (50-min average values) after interpolation to the current position of the *i*-th sound particle. The components u', v', w' represent the turbulent deviation from the mean wind field. The simulated turbulent kinetic energy $\overline{E}$ is used to control a synthetic turbulence generator which determines random realizations of u', v', w' so that spherical eddies are created which superimpose the mean flow and whose amplitude and size distribution statistically fulfil the local $\overline{E}$ and Kolmogorov's $k^{-5/3}$ law, respectively. The generator is used instead of loading a high number of instantaneous wind fields from the LES results. Turbulent fluctuations of the temperature are not considered. For the given wind speed they do not contribute significantly to the turbulent deviations from the mean effective sound speed $\overline{c} + \overline{u}$ in x-direction. A detailed description of the turbulence generator can be found in Section 3 of Heimann and Blumrich [14]. This parameterization accounts for the time-average effect of turbulence on refraction. Scattering by turbulence and turbulence-induced temporal fluctuations of the sound level are not simulated. Comparisons between the application of the turbulence generator and instantaneous LES realizations (snap shots) resulted in less than 0.3 dB difference of the mean sound level (Heimann et al. [15]).

3.2 *Sound emission*

Three source points are defined to represent the aeroacoustic sound emission of the three-blade rotor. The source points are 5 m away from the blade tip positions. Simulations are performed for twelve rotor angles (0°, 10°, ..., 110°) to describe a 1/3 revolution. Because the three blades are identical these simulations represent the full circle of source positions (Fig. 6). The considered frequencies cover all 1/3-octave bands from 20 Hz to 16 kHz, represented by the centre frequencies. The emission spectrum corresponds to Deutsche WindGuard [7]. The source points are assumed to be incoherent so that the phase can be disregarded when the sound level is determined in the receiver volumes.

The directivity of the source is set according to Ffowcs Williams and Hall [11] as cited by Oerlemans [28]. In this approach the directivity does not depend on frequency.

$$\Delta L_{\mathrm{dir}} = 10\lg\left(\sin^2(0.5\,\vartheta)\,\sin(\varphi)\right) \tag{8}$$

with

$$\varphi = \operatorname{acos}\left(-\left(n_x\,b_{21} + n_y\,b_{22} + n_z\,b_{23}\right)\right)$$

$$\vartheta = \pi - \operatorname{acos}\left(-\left(n_x\,b_{11} + n_y\,b_{12} + n_z\,b_{13}\right)\right)$$

$$b_{11} = 0\ ;\ b_{12} = \cos(\gamma)\ ;\ b_{13} = \sin(\gamma)$$

$$b_{21} = 0\ ;\ b_{22} = -b_{13}\ ;\ b_{23} = b_{12}$$

$$\gamma = \operatorname{acos}\left(\frac{z - z_{hub}}{r_s}\right)$$

z is the actual height of the source, z_{hub} the hub height, and r_s is the distance between the source point and the hub with $r_s = 0.9\,r$, where r is the radius of the rotor. The unity vector $\vec{n} = (n_x, n_y, n_z)$ defines the direction of emission, i.e. it is the starting vector of a sound ray.

Variations of the emission due to turbulent inflow (blade-vortex interactions) or varying blade and rotor parameters are not considered. The same applies to non-aeroacoustic sound (servo drives, generator noise).

3.3 *Sound propagation*

The acoustical domain size is confined by $0 \leq x \leq 2000$ m (length), $-200\ \mathrm{m} \leq y \leq +200$ m (width), and $0 \leq z - h \leq 250$ m (height); cf. Fig. 1. The height ensures that all particles, even those from high source positions and in downward refraction do not leave the domain through its upper lid before they reach ground-based receivers within the computational domain.

4,000,000 sound particles are used per source point. The sound particles are not emitted into the full space, but only into those directions that send the particles towards receiver volumes inside the model domain. Depending on the source position the starting direction of the particles (relative to the x-axis) ranges between $-64.5°$ and $+64.5°$ horizontally and between $-55.4°$ and $+27.6°$ vertically. The particles are traced with a time step of $\Delta t = 0.003$ s until they have left the computational domain. For a sound speed of $c = 340$ m/s this time step corresponds to spatial steps of 1 m length. The spherical receiver volumes have a diameter of 5 m. The volume centres are equidistant with a spacing of $\Delta x = \Delta y = \Delta z = 5$ m.

During their travel in the air the particles continuously lose sound energy due to air absorption. This process is parameterized according to ISO 9613-1 [19] as a function of frequency and temperature $\overline{T}$. As the relative humidity is not provided by the flow model a standard value, 70 percent, is assumed. Particles which hit the ground are reflected, i.e. they change their direction (specular reflection), lose a part of their energy and change their attributed phase according to the complex impedance of the ground Z_G, the grazing angle ϕ, and the plane-wave reflection coefficient

$$R = \frac{\sin\phi - \beta}{\sin\phi + \beta} \quad \text{with} \quad \beta = \frac{\overline{\rho}\,\overline{c}}{Z_G} \tag{9}$$

where $\overline{\rho} = p_0/(R_d\overline{T})$ is the mean density of air. The impedance ratio β is parameterized by the flow resistivity of the ground σ and the frequency according to Delany and Bazley [6], with $\sigma = 300$ kPa s m^{-2}, typical of dense soil, in the whole domain and for all cases.

3.4 Studied cases and model output

Simulations were performed for each of the four diurnal situations (00, 05, 12, 18 LT) and, in addition, for an idealized situation with a non-refractive atmosphere. For each of the five situations twelve simulations refer to varying rotor angles (0°, 10°... 110°). Each simulation considers the emission of all three blades for all 1/3-octave bands from 20 Hz to 16 kHz. In total, 5 × 12 simulations were performed.

The mean meteorological fields ($\overline{u}$, $\overline{v}$, $\overline{w}$, $\overline{c}$) only change with the diurnal situation. They are kept for the varying rotor angles, while turbulent wind fluctuations (u', v', w') are added to the mean fields. The components u', v', w' are randomly changed during the simulation time, i.e. the travel time of the particles. The procedure is described in Section 4 in [13]. The emitted sound power of the source, i.e. the total over all emission angles, and its distribution to the emission angles (directivity) is held for all simulations. The same applies to the ground impedance. This allows to isolate the meteorological propagation effects.

Each single simulation assumes that the rotor is fixed at the given rotor angle position and sound is emitted until a steady state sound level is achieved at all receivers. This assumption is necessary because the travel time of the sound waves from the three blades to a specific receiver varies with the length and course of the contributing sound rays (e.g. direct or ground-reflected rays). Near the turbine ($x \leq 200$ m) the spent travel times vary by 0.15 to 0.30 s. Given a rotor speed of eight rotations per minute this means that coincidently arriving sound waves at a receiver have been emitted at the sources while the rotor has turned by up to 14°. Therefore a sequence of results with increasing rotor angle cannot be unconditionally interpreted as a dynamic time-dependent sound-level prediction. Nevertheless, the results can be used to roughly assess the locally received amplitude modulation as far they are caused by the modelled processes, i.e. source directivity and propagation effects (refraction, ground reflection, and air absorption) in a steady state atmosphere.

All model results discussed in the following are A-weighted sound levels $\overline{L}_A$ of the lowest layer of receiver volumes with centres 2.5 m above the ground surface. They are calculated from the partial sound levels for the centre frequencies of all 1/3-octave-bands from 20 Hz to 16 kHz. The corresponding sound levels resulting from the simulations for a non-refractive atmosphere are referred to as $\overline{L}_{A,nr}$. $\overline{L}_A$ and $\overline{L}_{A,nr}$ are calculated for single rotor angles. They have to be interpreted as being averaged over the time scale of turbulence. In addition, energy-equivalent mean sound levels are calculated over all twelve rotor angles. The latter represent average sound levels over a full rotation for the given meteorological situation and are denoted as $\hat{L}_A$ and $\hat{L}_{A,nr}$. To isolate the effect of refraction the relative sound levels $\overline{L}_A - \overline{L}_{A,nr}$ and $\hat{L}_A - \hat{L}_{A,nr}$ are evaluated in the following sections.

3.5 Tests

Two problems which are associated with the chosen model layout are addressed in two-dimensional test runs in the *x*-*z*-plane for *y*=0 with all velocity components and gradients in *y*-direction being set to zero. The test runs refer to the 00 and 12 LT situations and source heights 50, 100 to 150 m above ground.

(a) Since the particle model is based on ray acoustics which in turn is a high-frequency approximation, we performed test runs for all 1/3-octave band from 20 Hz to 16 kHz and alternatively for the 1/3-octave bands from 100 Hz to 16 kHz. Omitting the lowest seven frequency bands leads to maximum deviations of the relative sound level $\overline{L}_{\mathrm{A}} - \overline{L}_{\mathrm{A,nr}}$ of only 0.2 dB compared to the full spectrum. This applies to all tested configurations. Hence, it is concluded that considering the full source spectrum does not impair the results.

(b) The application of the impedance parameterization of Delany and Bazley [6] or alternative one-parameter models, e.g. Miki [27], to outdoor ground surfaces became subject to critics in the last years, cf. Dragna and Blanc-Benon [8]. Therefore, two-dimensional test runs were performed for rigid, i.e. totally reflecting ground. This eliminates the use of a parameterization. In most cases the results for rigid ground do not deviate by more than 0.5 dB from those for the finite impedance ground as parameterized using [6] for $\sigma = 300$ kPa s m^{-2}. Only for a low source position (50 m above ground) and $x > 1400$ m larger deviations of up to 5 dB were obtained. Since the present study does not intend to investigate the influence of different ground properties, the simulations of the present study are based on [6] for compatibility with earlier studies without expecting impairments of the findings.

3.6 Results

This section deals with the results of the acoustic simulations in a rather descriptive way. Interpretations, comparisons and discussions of all results are summarized in Section 4.

First, results for specific rotor angles are considered. As the rotor revolves the source positions vary and the sound rays that contribute to the local sound impact change their course towards the receivers. Hence, they encounter varying gradients of sound speed and wind and thus experience changing refraction. The influence of the rotor angles on the near-ground sound level is shown in Fig. 7 by way of example for the midnight situation 00 LT. The complex structure of the downwind atmosphere leads to focusing and defocusing of the sound rays resulting in zones enhanced and diminished sound levels. The patterns are changing as the rotor spins around, especially at distant positions ≥ 500 m .

The distributions of $\overline{L}_A - \overline{L}_{A,nr}$ are the consequence of what the sound waves have experienced during their propagation from the elevated source points to the near-ground receivers. As Fig. 4 suggests, the sound waves pass zones with upward and downward refraction. In addition come sideward and slant refractions (Fig. 5). Descriptive ray patterns as they result from two-dimensional simulations (for instance Fig. 6 in Heimann et al. [17]) can be hardly pictured in three dimensions. Instead, Fig. 8 gives an impression of the three-dimensional effects. The shaded-surface graphs show that elongated and entangled zones with focusing or even caustics exist where refraction locally increases the sound level by more than 9 dB. The red-shaded contours in Fig. 7 indicate where these zones touch the ground.

The average sound levels over a full rotation are calculated as the energy-equivalent average sound levels $\hat{L}_A$ over the twelve rotor positions. As Fig. 9 reveals, the relative sound levels $\hat{L}_A - \hat{L}_{A,nr}$ show rather different patterns of refraction effects near the ground during the course of the day. During stable stratification (at 00 and 05 LT) the distributions are asymmetric with respect to the x-axis because the wind direction turns with height. At 12 and 18 LT when the stratification is unstable or neutral the wind barely veers and the patterns of the relative sound level are more symmetric with respect to the x-axis. Refraction causes weak to moderate enhancement (3 to 6 dB) in elongated zones with areas of diminishment (0 to -3 dB) in between. Under unstable conditions (12 LT) the wake of the turbine is rather short and the sound level enhancement due to refraction is weak (up to 3 dB) and restricted to the medium range (600 m $\leq x \leq 1400$ m). At 18 LT refraction causes a marked hairpin-shaped increase of the near-ground sound level by more than 9 dB, locally up to 18 dB. Beyond $x = 1500$ m a zone forms near the x-axis where the sound level drops by more than 12 dB below the level of a non-refractive atmosphere. It is the consequence of defocusing. The three-dimensional structure of this pattern is shown in Fig. 10. It discloses that the enhancement zone starts near the ground at about $x = 500$ m, where a tube-like structure extends in downwind direction with increasing vertical thickness. The pattern suggests that ground reflection significantly contributes to the focusing which leads to enhancement.

Fig. 11 presents horizontal profiles along the x-axis of the near-ground A-weighted sound level $\hat{L}_A$ averaged over all rotor angles. To be independent of the source strength the graphs refer to the relative sound level $\hat{L}_A - \hat{L}_{A,100}$, where $\hat{L}_{A,100}$ is the corresponding value at $x = 100$ m. Within the first 800 m from the turbine the sound level decreases continuously. Up to x = 500 m the simulated sound levels are not much influenced by refraction as they agree with the results of the reference simulation for a non-refractive atmosphere. Beyond x = 500 m the curves separate as a consequence of refraction. At x = 800 m $\hat{L}_A - \hat{L}_{A,100}$ varies by about 6 dB during the course of the day where the levels for 00 and 05 LT (stable boundary layer) are lower than those for 12 LT and 18 LT (convective and neutral boundary layer). Between $x = 800$ m and x = 1500 m $\hat{L}_A - \hat{L}_{A,100}$ exceeds the curve for the non-refractive reference for all situations except for 00 LT. A particularly high rise is simulated for the evening situation at 18 LT when the level at x = 1250 m even reaches the near-field value at x = 200 m. Finally, beyond x = 1500 m all curves drop below the non-refraction reference curve.

Eventually, the variation of the sound level during one rotation of the turbine is addressed. The amplitude modulation as a time-dependent phenomenon cannot be directly analysed in the model results as explained in Section 3.4. However, if the sound level is evaluated as a function of the rotor angle with the assumption of steady-state results for each single rotor angle, the amplitude of the local sound level during a rotation can be at least estimated. Note that the simulated influence of the rotor angle only includes variations of the source-receiver distance, the source directivity and the refraction encountered during propagation. Temporal variations of the emission and the turbulent wind field also contribute to amplitude variations in reality, but they are not considered in this study.

The sound-level variation during the revolution of the rotor is shown in Fig. 12 for two distances. At x = 400 m sound levels vary by about 4 dB. A smaller variation (approx. 2 dB) is simulated for the convective 12 LT situation. The variation of the reference sound level for a non-refractive atmosphere is much smaller and indicates that the variation at this distance can be mainly attributed to refraction. In the far field at $x = 1200$ m the sound-level variation is much larger, chiefly for the morning and evening hours (05 and 18 LT). At 18 LT the variation width reaches more than 36 dB and the peaks almost attain the near-field value of the average over all rotor angles at $x = 100$ m.

Fig. 13 shows the horizontal distribution of the excess sound level during one rotation, i.e. the difference between the peak sound level and the average sound level over all rotor angles, $\overline{L}_{A,\max} - \hat{L}_A$. Only near the source ($x \leq 500$ m) the maximum excess sound level is concentrated near the centre line (y = 0). Farther away also lateral areas are affected. The highest excess sound levels are simulated for 18 LT in the far field for $x \geq 1200$ m.

4. Discussion

The relevance of the attained results is discussed in this section. The results are examined with respect to the role of the wake and the atmospheric stability on the sound field. They are compared with the recently published results in Larsson and Öhlund [23], Barlas et al. [1] and Barlas et al. [2].

The principle simulation setup of our study resembles that of [1] and [2]: Acoustic simulations are performed on large-eddy simulation output. This approach accounts for the influence of a wind turbine on the meteorological environment of the sound waves propagating from the turbine to near-ground receivers. In detail, there are some important differences which have to be taken into consideration when comparing the results: The main difference in the flow simulations concerns the upstream velocity perturbations. While [2] applied a pre-generated turbulent wind field (Mann [25]), scaled in order to mimic the different turbulence intensity levels, Englberger and Dörnbrack [10] extracted synchronized upstream velocity perturbations at each time step directly from a diurnal cycle precursor LES run. Further, the wind turbine drag is parameterized by the actuator disc concept in our study while the actuator line approach is used by [1] and [2]. As for the implementation of the sound source the degree of sophistication in our study is between the rather simple parameterization in [1] and the more advanced one in [2]. We use a standard source frequency spectrum, consider source directivity, and one fixed source point per blade. All source parameters are kept constant between the cases. The dimensions of the wind turbine and the meteorological situations differ slightly between our study and [1], [2].

The main difference between the studies consists in the type of acoustical modelling. While [1] and [2] use a two-dimensional parabolic equation (PE) model which they apply along selected vertical slices, we rely on a fully three-dimensional sound particle model. On the one hand the PE approach is superior because it accounts for refraction, ground reflection and diffraction for all frequencies, while the ray-based particle model is a high-frequency approximation, i.e. low-frequency waves cannot be accurately simulated near strong atmospheric gradients and in caustics. On the other hand the three-dimensional particle model considers refraction in all directions. In many cases of outdoor sound propagation it is well justified to neglect horizontal refraction because the main gradients in the atmospheric boundary layer are vertically oriented except those in transient turbulent eddies. However, in the wake of a wind turbine horizontal and vertical gradients have the same magnitude, even those of the average atmospheric parameters, i.e. $\overline{u}$, $\overline{v}$, $\overline{w}$, $\overline{c}$.

The studies largely agree with regard to the simulated wind fields. The wind speed deficit in the wake is more elongated in stable situations than it is in an unstable (convective) boundary layer where turbulence causes a quick mixing and erosion of the wake deficit. There are also similarities in the simulated sound-level fields. From the turbine downstream to a distance of approx. 1000 m the sound level steadily drops. This decrease is more pronounced in stable stratification than in unstable (convective) stratification (compare Fig. 8 in [1] with Fig. 11 here). Beyond a distance of 1000 m the results differ although some features are still similar. In [1] a sudden increase of the sound level is simulated where focused and downward refracted sound waves hit the ground. The location of the onset depends on stability. From stable via neutral through to convective stratification the onset is shifted streamwise. In our simulations there is a similar rise of the sound levels, but it is only found for slightly stable and near-neutral stratification at 05 and 18 LT. For the convective case (12 LT) there is no rise down to a distance of 2000 m. In Barlas et al. [1] the rise for the convective boundary layer starts already somewhat before 2000 m, but the maximum is only behind our domain limit at x = 2000 m. The differences in the positions of the far-field increase of the sound levels are possibly caused by the different size of the turbine ($z_{\mathrm{hub}} = 80$ m vs. $z_{\mathrm{hub}} = 100$ m and $r = 40$ m vs. $r = 50$ m) and the different large-scale wind speed (12 m/s vs. 10 m/s). As shown by [1] the onset of the far-field rise is shifted towards the turbine as the incoming wind speed increases. A smaller sized wind turbine should also shift the rise towards the source. This partly explains the differences. Other discrepancies may originate from three-dimensional effects. In contrast to [1] the results of Cotté [5] do not show major differences between neutral, stable and unstable stratification in the downwind area ($0 < x \leq 1200$ m). Maybe this is because the variation of the vertical temperature profiles is rather small and almost no inversion and low-level wind maximum are showing up in the stable case.

In comparison to [2], who applied 'quasi-3D' propagation simulations, i.e. vertically two-dimensional simulations in selected radial slices and subsequent horizontal interpolation, the fully three-dimensional results show rather different horizontal patterns of the sound level for neutral stratification (Fig. 12 in [1] upper row compared with Fig. 9 for 18 LT here). In particular, the 3-dim simulations generate narrow longish zones of amplified sound levels. These are not visible in the interpolated 2D results of [2]. This feature is attributed to the three-dimensional, i.e. vertical, horizontal, and slant refraction.

Asymmetric sound-level distributions as they result in the stable cases (Fig. 9; 00 and 05 LT) are caused by the vertical veering of the wind (Ekman effect). To capture this effect again fully three-dimensional simulations are required.

As for the amplitude modulation (AM) Larsson and Öhlund [23] found from measurements in Sweden that at a distance of 400 m ('Ryningsnäs site') most AM events appear in evening and morning hours and during night. This agrees with our results which show that at this distance the amplitude variation due to varying rotor angles is smallest for the day-time situation at 12 LT (cf. Fig. 12). At another observation site ('Dragaliden site') the distance from the turbine is about 1200 m. Here the reported amplitude modulation is even more frequent during stable stratification.

The high modulation depth that is simulated at $x = 1200$ m for 05 and 18 LT of 24 and even 36 dB could not be verified in literature. Partly it may result from overestimated focusing of low-frequency waves which is inherent in ray-based models. Nevertheless, modulation depths of up to 15 dB were definitely reported (e.g. Ioannidou et al. [18]). In many real outdoor situations the sound-level minima in the far field are masked by background noise which is not considered in the present simulations. Given a near-field averaged sound-level of $\hat{L}_{A,100} = 50$ dB and a background noise level of 30 dB then intermittent sound from the turbine would exceed the background noise by only 8 and 18 dB at 05 and 18 LT, respectively. This better fits in with the observed magnitude.

5. Conclusion

From the results of the simulations it can be concluded that the sound level in the downwind domain of a single wind turbine is highly modified by the complex refraction in the wake which varies during the course of the days. Sound waves are passing regions with downward, upward and sideward refraction so that sound rays may be converging and diverging successively. This leads to local focusing and even caustics and corresponding sound-level enhancements which can also affect the sound level near the ground. As the meteorological conditions change and thereby modify the shape of the wake the refraction patterns change accordingly and regions of amplified sound impact shift to other places, do not reach the ground anymore or even disappear. It was already shown by Heimann et al. [17] that sound propagation through the wake of a wind turbine is very sensitive to rather small changes in the meteorological fields.

But also for a given time of the day, i.e. a fixed meteorological situation, the sound sources at the rotating blades continuously move so that the sound rays towards a receiver pass through varying regions of refraction. This leads to local oscillations of the sound level in the far field where the typical near-field fluctuations due to directivity and varying distance are no longer important.

Moreover, it can be concluded that three-dimensional refraction effects are important. This is particularly the case in stable conditions when the wind direction turns with height. This leads to an asymmetric distribution of the sound impact with respect to the streamwise centre line.

In the future it is necessary to supplement numerical simulations with field measurements. Well-instrumented research wind farms, with meteorological and acoustical sensors, covering wake and far field, and controlled and documented operations, are about to become available for research and will overcome the present lack in data.

Acknowledgements

This research was performed as part of the LIPS project, funded by the German Federal Ministry for Economic Affairs and Energy under grant no. 0325518 by a resolution of the German Federal Parliament. The authors gratefully acknowledge the Gauss Centre for Supercomputing e.V. (www.gauss-centre.eu) for supporting this project by providing computing time on the GCS Supercomputer SuperMUC at Leibniz Supercomputing Centre (LRZ, www.lrz.de) in Garching near Munich.

References

[1] Barlas E, Zhu WJ, Shen WZ, Kelly M, Andersen SJ. Effects of wind turbine wake on atmospheric sound propagation, Applied Acoustics 2017a; 122 : 51-61. DOI: 10.1016/j.apacoust.2017.02.010.

[2] Barlas E, Zhu WJ, Shen WZ, Dag KO, Moriarty P. Consistent modelling of wind turbine noise propagation from source to receiver, J. Acoust. Soc. Am. 2017b; 142 : 3297-3310. DOI: 10.1121/1.5012747.

[3] Bingöl F, Mann J, Larsen GC. Light detection and ranging measurements of wake dynamics. Part I: one-dimensional scanning, Wind Energy 2010; 13 : 51-61. DOI: 10.1002/we.352

[4] Branlard E. Wind Turbine Aerodynamics and Vorticity-Based Methods. Springer Publishers 2017, DOI: 10.1007/978-3-319-55164-7. ISBN: 978-3-319-55163-0.

[5] Cotté B. Coupling of an aeroacoustic model and a parabolic equation code for long range wind turbine noise propagation. J. Sound Vib. 2018; 422: 343-357. DOI: 10.1016/j.jsv.2018.02.026.

[6] Delany ME, Bazley EN. Acoustical properties of fibrous absorbent materials, Applied Acoustics 1970; 3 : 105-116. DOI: 10.1016/0003-682X(70)90031-9.

[7] Deutsche WindGuard GmbH. Schallemissionsmessungen an einer Windenergieanlage. Bericht MN15016.A1, 2015; 49 pages.

[8] Dragna D, Blanc-Benon P. Physically admissible impedance models for time-domain computations of outdoor sound propagation. Acta Acustica united with Acustica 2014; 100: 401-410. DOI 10.3813/AAA.918719.

[9] Englberger A, Dörnbrack A. Impact of neutral boundary-layer turbulence on wind-turbine wakes: A numerical modelling study. Boundary-Layer Meteorol. 2017a; 162 : 427-449. DOI: 10.1007/s10546-016-0208-z

[10] Englberger A, Dörnbrack A. Impact of the diurnal cycle of the atmospheric boundary layer on wind-turbine wakes: A numerical modelling study. Boundary-Layer Meteorol. 2017b; DOI: 10.1007/s10546-017-0309-3.

[11] Ffowcs Williams JE and Hall LH. Aerodynamic sound generation by turbulent flow in the vicinity of a scattering half plane. J. Fluid Mech. 1970; 40 : 657-670.

[12] Gebraad PMO, Teeuwisse FW, van Wingerden JW, Fleming PA, Ruben SD, Marden JR, Pao LY. Wind plant power optimization through yaw control using a parametric model for wake effects—a CFD simulation study. Wind Energy 2016; 19: 95-114. DOI: 10.1002/we.1822.

[13] Gross G. Numerical simulations to the diurnal variation of wakes behind wind turbines. Meteorol. Z. 2010; 19: 91–99. DOI: 10.1127/0941-2948/2010/0418.

[14] Heimann D, Blumrich R. Time-domain simulations of sound propagation through screen-induced turbulence. Applied Acoustics 2004; 65 : 561-582. DOI: 10.1016/j.apacoust.2003.09.007

[15] Heimann D, Englberger A, Schady A. Sound propagation through the wake flow of a hilltop wind turbine—A numerical study. In print. DOI: 10.1002/we.2185

[16] Heimann D, Gross G. Coupled simulation of meteorological parameters and sound intensity in a narrow valley. Applied Acoustics 1999; 56 : 73-100. DOI: 10.1016/S0003-682X(98)00018-8.

[17] Heimann D, Käsler Y, Gross G. The wake of a wind turbine and its influence on sound propagation. Meteorologische Zeitschrift 2011; 20 : 449-460. DOI: 10.1127/0941-2948/2011/0273

[18] Ioannidou C, Santurette S, Jeong C-H. Effect of modulation depth, frequency, and intermittence on wind turbine noise annoyance. J. Acoust. Soc. Am. 2016; 139 : 1241-1251. DOI: 10.1121/1.4944570

[19] ISO 9613-1. Acoustics; attenuation of sound during propagation outdoors; part 1: calculation of the absorption of sound by the atmosphere. 1993.

[20] Jimenez A, Crespo A, Migoya E, Garcia J. Advances in large-eddy simulation of a wind turbine wake. Journal of Physics: Conference Series 2007: 75 : 012041. DOI: 10.1088/1742-6596/75/1/012041

[21] Käsler Y, Rahm S, Simmet R. Wake measurements of a multi-MW wind turbine with coherent long-range pulsed Doppler wind lidar. J. Atmos. Oceanic Technol. 2010; 27 : 1529-1532, DOI: 10.1175/2010JTECHA1483.1

[22] Kim H, Lee S, Son E, Lee S, Lee S. Aerodynamic noise analysis of large horizontal axis wind turbines considering fluid–structure interaction. Renewable Energy, 2012; 42 : 46-52. DOI: 10.1016/j.renene.2011.09.019

[23] Larsson C, Öhlund O. Amplitude modulation of sound from wind turbines under various meteorological conditions. J. Acoust. Soc. Am. 2014; 135 : 67-73. DOI: 10.1121/1.4836135

[24] Lee S, Lee D, Honhoff S. Prediction of far-field wind turbine noise propagation with parabolic equation. J. Acoust. Soc. Am. 2016; 140: 767–778. 10.1121/1.4958996.

[25] Mann J. Wind field simulation. Prob. Engng. Mech. 1998; 13: 269-282. DOI: 10.1016/S0266-8920(97)00036-2.

[26] Margolin LG, Smolarkiewicz PK, Sorbjan Z. Large-eddy simulations of convective boundary layers using nonoscillatory differencing. Physica D: Nonlinear Phenomena 1999; 133: 390-397.

[27] Miki Y. Acoustical properties of porous materials – modifications of Delany-Bazley models. J.Acoust.Soc.Jpn. 1990; 11 : 19-28.

[28] Oerlemans S. Wind turbine noise: primary noise sources. Nationaal Luchten Ruimtevaartlaboratorium, report NLR-TP-2011-066, 2011; 57 pages

[29] Pedersen E, van der Berg F, Bakker R, Bouma J. Response to noise from modern wind farms in The Netherlands. J. Acoust. Soc. Am. 2009; 126 : 634-643. DOI: 10.1121/1.3160293

[30] Pierce A.D. Acoustics – An introduction to its physical principles and applications. McGraw-Hill Inc.: New York, 1981; 1-619.

[31] Prusa JM, Smolarkiewicz PK, Wyszogrodzki AA. EULAG, a computational model for multiscale flows. Computers & Fluids 2008; 37 : 1193–1207. DOI: 10.1016/j.compfluid.2007.12.001

[32] Rogers AL, Manwell JF, Wright S. Wind turbine acoustic noise. A white paper prepared by Renewable Energy Research Laboratory, University of Massachusetts 2006; Obtainable from http://www.ceere.org.

[33] Schmidt H, Schumann U. Coherent structure of the convective boundary layer derived from large-eddy simulations. J. Fluid Mech. 1989; 200: 511-562. DOI: 10.1017/S0022112089000753.

[34] Smolarkiewicz PK, Margolin LG. MPDATA: A Finite-Difference Solver for Geophysical Flows. J. Comput. Phys. 1998; 140 : 459–480. DOI; 10.1006/jcph.1998.5901.

[35] Sørensen JN, Mikkelsen RF, Henningson DS, Ivanell S, Sarmast S, Andersen SJ. Simulation of wind turbine wakes using the actuator line technique. Phil. Trans. R. Soc. A 2015; 373: 20140071. DOI: 10.1098/rsta.2014.0071

[36] Tabassum-Abbasi, Premalatha M, Abbasi T, Abbasi SA. Wind energy: Increasing deployment, rising environmental concerns. Renewable and Sustainable Energy Reviews 2014; 31 : 270-288. DOI: 10.1016/j.rser.2013.11.019

[37] Troldborg N, Sørensen JN, Mikkelsen R. Numerical simulations of wake characteristics of a wind turbine in uniform inflow. Wind Energy 2010; 13 : 86-99. DOI: 10.1002/we.345

[38] Trujillo JJ, Bingöl F, Larsen GC, Mann J, Kühn M. Light detection and ranging measurements of wake dynamics. Part II: two-dimensional scanning, Wind Energy 2011; 14 : 61-75. DOI: 10.1002/we.402

[39] Vermeer LJ, Sørensen JN, Crespo A. Wind turbine wake aerodynamics. Progress in Aerospace Sciences 2003; 39 : 467-510. DOI: 10.1016/S0376-0421(03)00078-2

[40] Wussow S, Sitzki L, Hahm T. 3D-simulations of the turbulent wake behind a wind turbine. Journal of Physics: Conference Series 2007; 75 : 012033. DOI: 10.1088/1742-6596/75/1/012033

Figure captions

Fig. 1: Plane view of the coordinate system (x, y) and position of the domains of the flow model (outer frame) and the sound propagation model (grey shaded). The grey arrow marks the main inflow wind direction. The position of the wind turbine is indicated by the black symbol in the origin (x=y=0).

Fig. 2: Vertical profiles of the simulated 50-min average sound speed $\overline{c}$ in the upwind area of the wind turbine at $x = -200$ m, $y = 0$. The line styles indicate the time of the day (LT = local time).

Fig. 3: Vertical profiles of the simulated mean wind components $\overline{u}$ and $\overline{v}$ upwind (at $x = -200$ m, $y = 0$, grey curves) and downwind (at $x = +200$ m, $y = 0$, black curves) of the wind turbine. The line styles indicate the time of the day (LT = local time).

Fig. 4: Vertical cross sections (x-z-plane through y=0) of the effective speed of sound $\overline{c}_{\mathrm{eff},x}$ for sound propagation in x-direction. The time of the day is indicated as local time (LT). The red bars show the vertical extent of the rotor plane.

Fig. 5: Vertical cross section ($y - z -$ plane at x = 400 m) of the spanwise gradient of the effective speed of sound $\overline{c}_{\mathrm{eff,x}}$ for the situation 00 LT. The arrows point into the direction of refraction, i.e. towards low values of $\overline{c}_{\mathrm{eff,x}}$. The position of the rotor plane is indicated by the broken circle.

Fig. 6: Geometry of the wind turbine, rotor angle, and positions of the sound sources at the rotor blades.. The turbine is seen from the downwind side (y-z-cross section through x=0).

Fig. 7: Near-ground (z=2.5 m) A-weighted sound pressure level relative to 'no refraction' ($\overline{L}_A - \overline{L}_{A,nr}$) for four rotor angles (from top to bottom: 0°, 30°, 60°, 90°).The results refer to the midnight situation (00 LT). The respective blade positions are sketched as they are seen from the downwind side.

Fig. 8: Surfaces enveloping locations with $\overline{L}_A - \overline{L}_{A,nr} \geq 9$ dB for two rotor angles: top: 0°, bottom: 60°. The results refer to 00 LT.

Fig. 9: Near-ground (z=2.5 m) A-weighted sound pressure level relative to 'no refraction' ($\hat{L}_A - \hat{L}_{A,nr}$) averaged over a full rotation for the time of the day as indicated (LT = local time).

Fig. 10: Surface enveloping locations with $\hat{L}_A - \hat{L}_{A,nr} \geq 9$ dB. The result refers to 18 LT.

Fig. 11: Horizontal profiles of the near-ground A-weighted averaged sound pressure levels $\hat{L}_A - \hat{L}_{A,100}$ along the x-axis (y = 0, z = 2.5 m). Line styles indicate the time of the day. The solid grey curve refers to a non-refractive atmosphere. The broken grey curve indicates free-field propagation from an idealized point source at the hub with a decay of approx. 6 dB per doubled distance.

Fig. 12: Local variation of the A-weighted sound level difference $\overline{L}_A - \hat{L}_{A,100}$ as a function of the rotor angle α at $x = 400$ m ;$y = 0$;$z = 2.5$ m (top) and $x = 1200$ m ;$y = 0$;$z = 2.5$ m (bottom). The line styles indicate the time of the day as in Fig. 11. The grey curves refer to a non-refractive atmosphere $\overline{L}_{A,nr} - \hat{L}_{A,nr,100}$. Note that the ordinates have different scales.

Fig. 13: Near-ground (z=2.5 m) difference between the maximum A-weighted sound pressure level during one rotation and the averaged A-weighted sound pressure level ($\overline{L}_{A,\max} - \hat{L}_A$) for the time of the day as indicated (LT = local time).

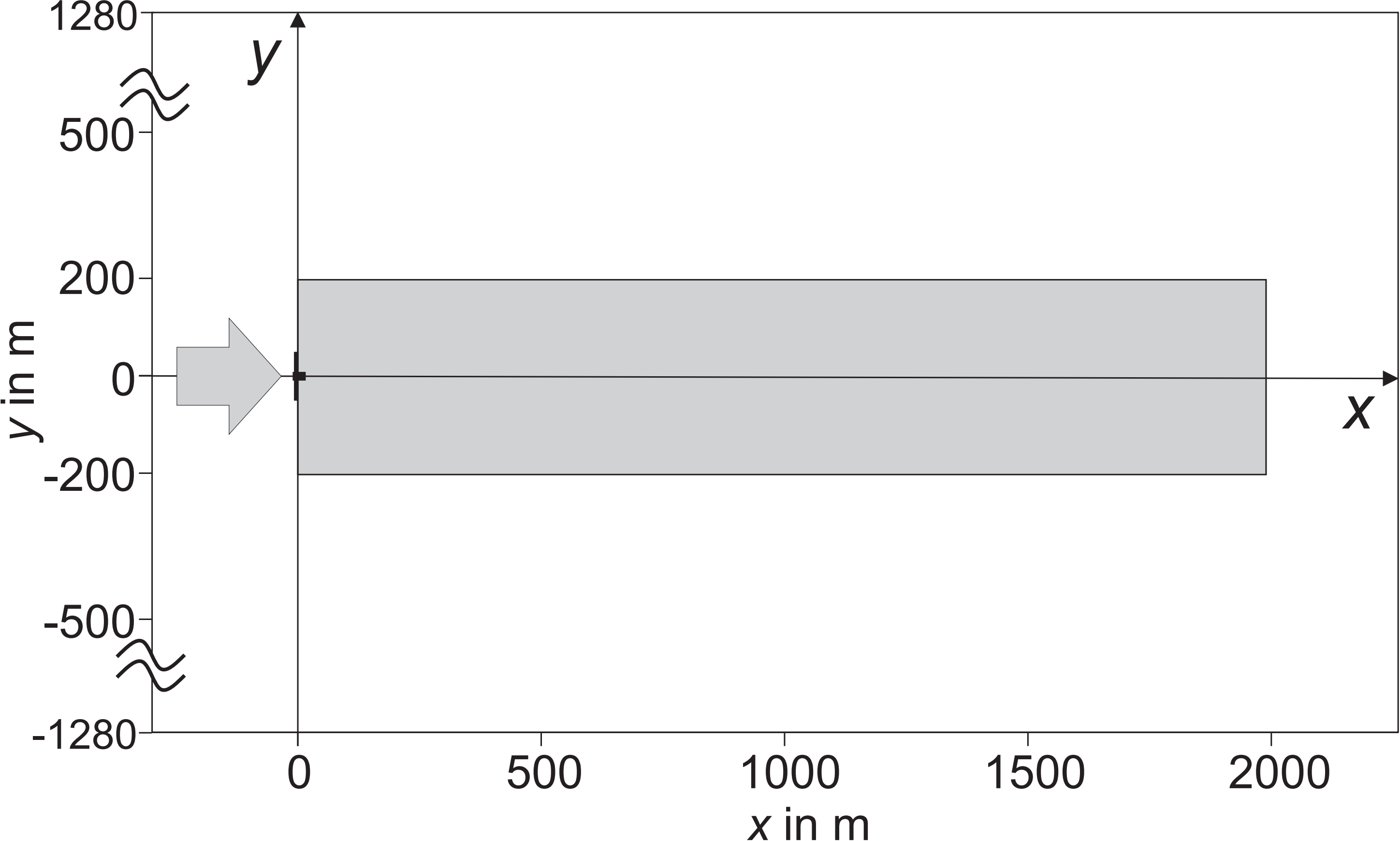

1280
500
200
0
-200
-500
-1280
y in m
y
x
0
500
1000
1500
2000
x in m

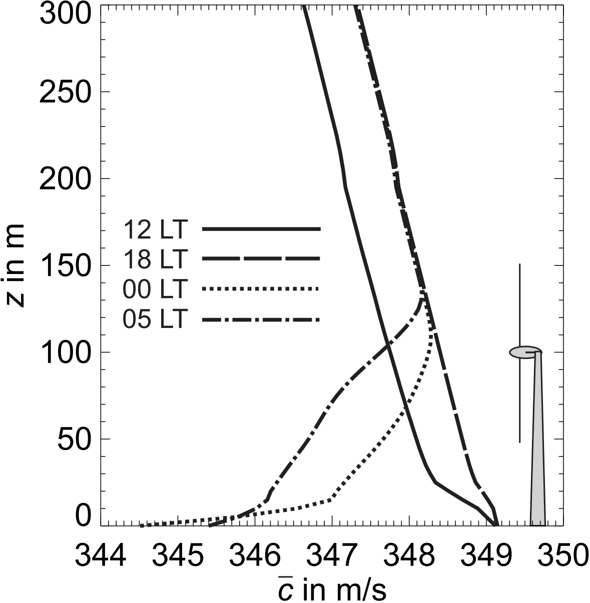

300
250
200
150
100
50
0
z in m
12 LT
18 LT
00 LT
05 LT
344
345
346
347
348
349
350
$\bar{c}$ in m/s

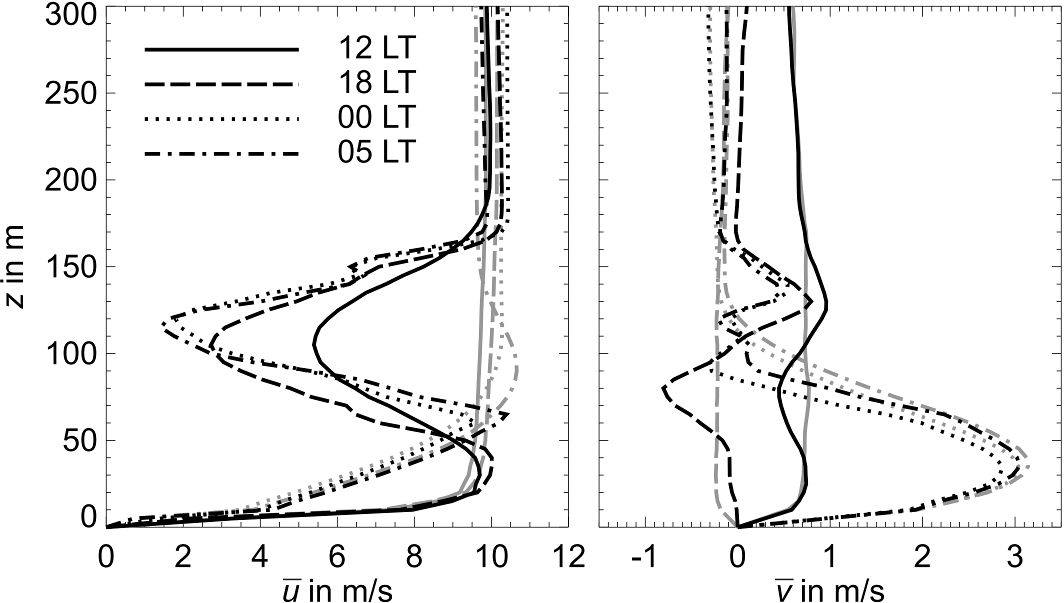

12 LT
18 LT
00 LT
05 LT
z in m
$\overline{u}$ in m/s
$\overline{v}$ in m/s
0
50
100
150
200
250
300
0
2
4
6
8
10
12
-1
0
1
2
3

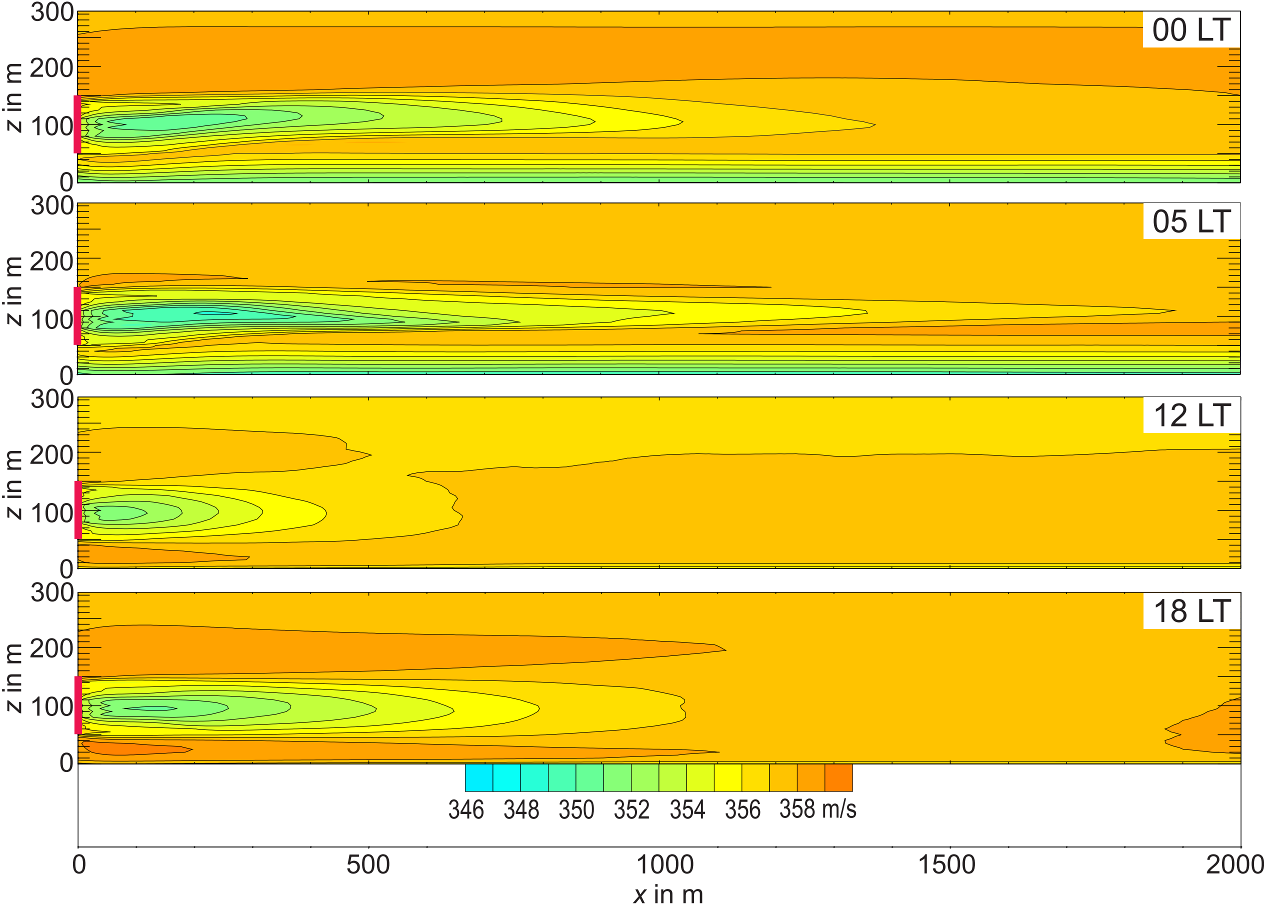

00 LT
05 LT
12 LT
18 LT
z in m
300
200
100
0
346
348
350
352
354
356
358 m/s
0
500
1000
1500
2000
x in m

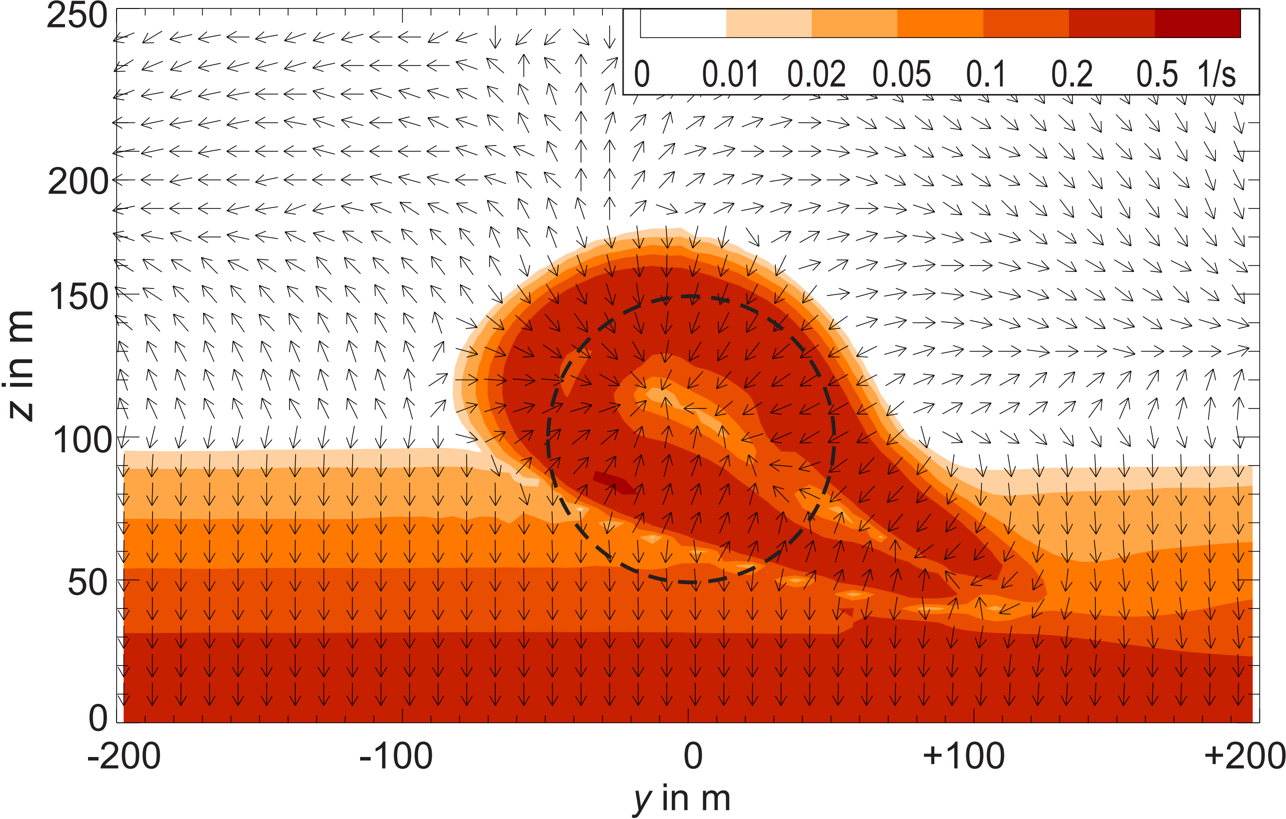

0
0.01
0.02
0.05
0.1
0.2
0.5
1/s
250
200
150
100
50
0
z in m
-200
-100
0
+100
+200
y in m

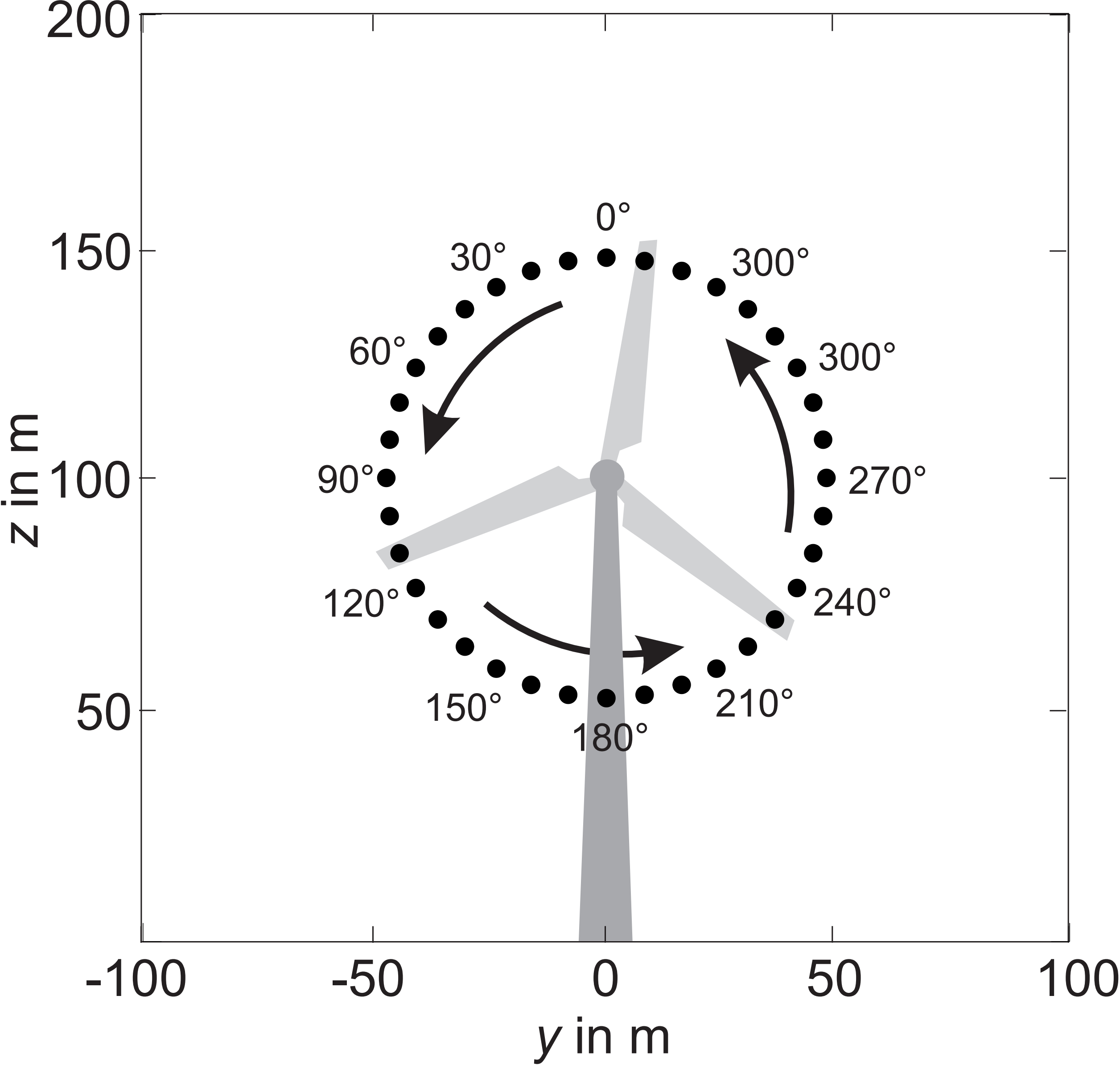
200
150
100
50
z in m
-100
-50
0
50
100
y in m
0°
30°
60°
90°
120°
150°
180°
210°
240°
270°
300°
300°

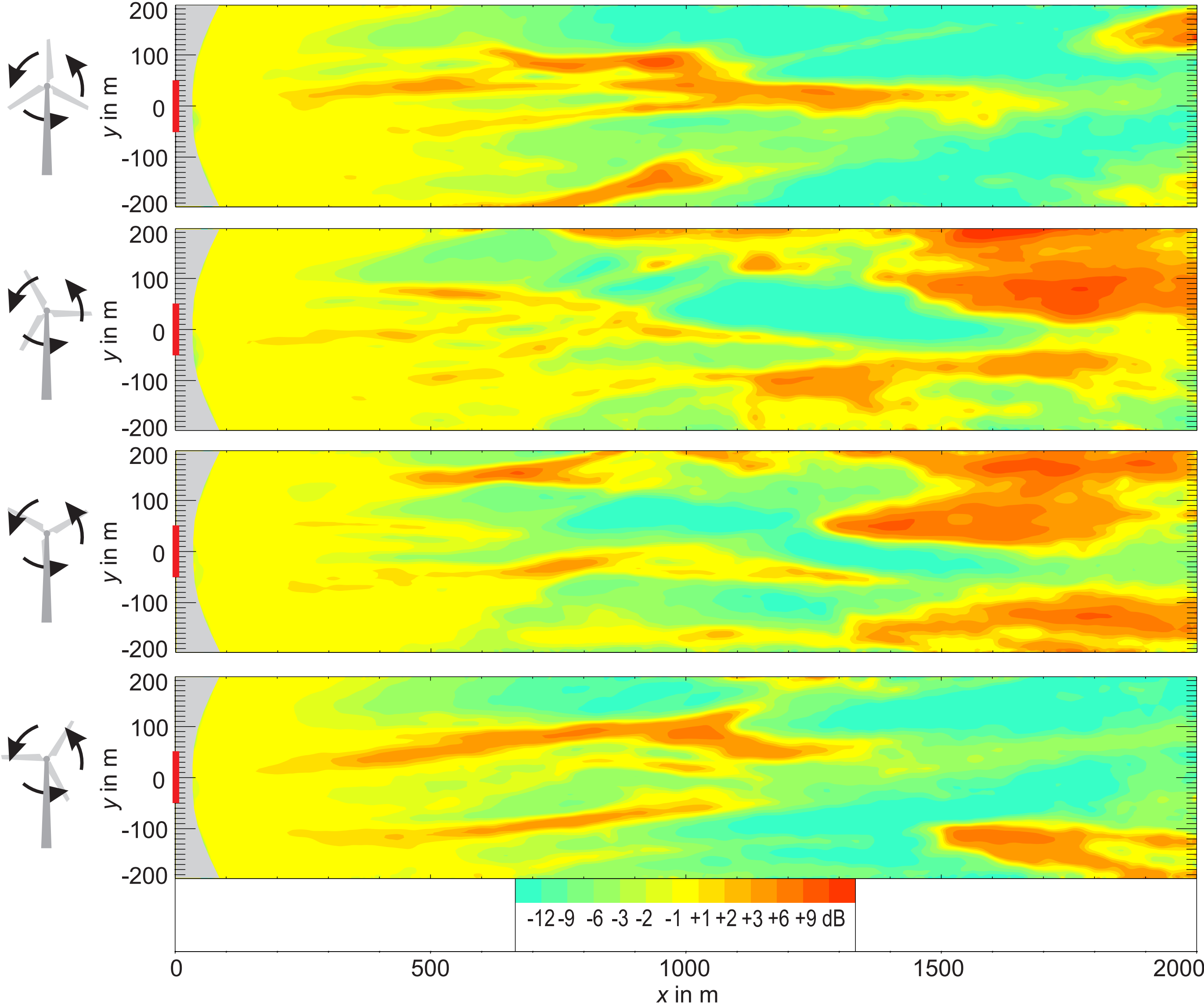

200
100
0
-100
-200
y in m
-12 -9 -6 -3 -2 -1 +1 +2 +3 +6 +9 dB
0
500
1000
1500
2000
x in m

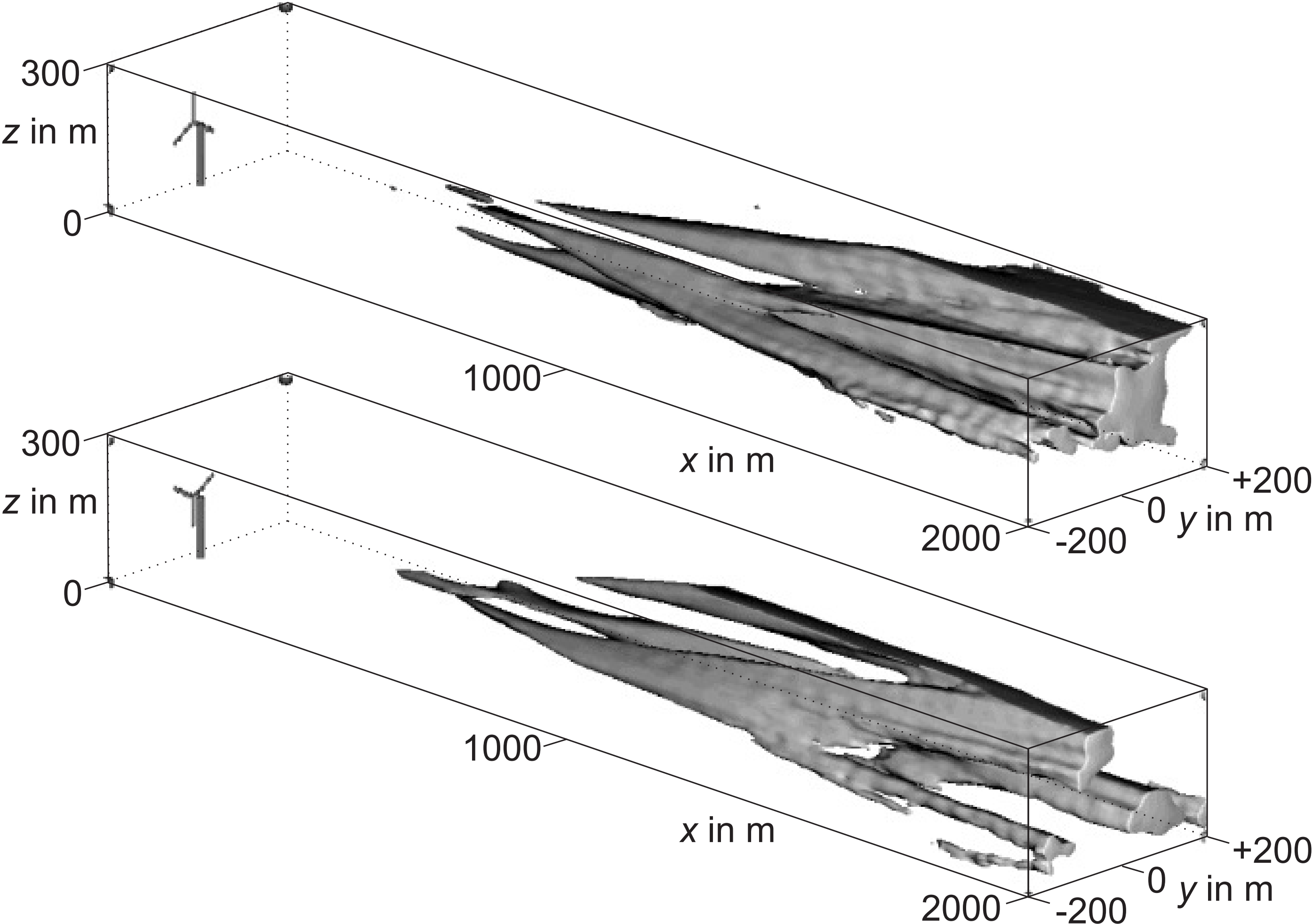

300
z in m
0
1000
x in m
2000
-200
0
+200
y in m
300
z in m
0
1000
x in m
2000
-200
0
+200
y in m

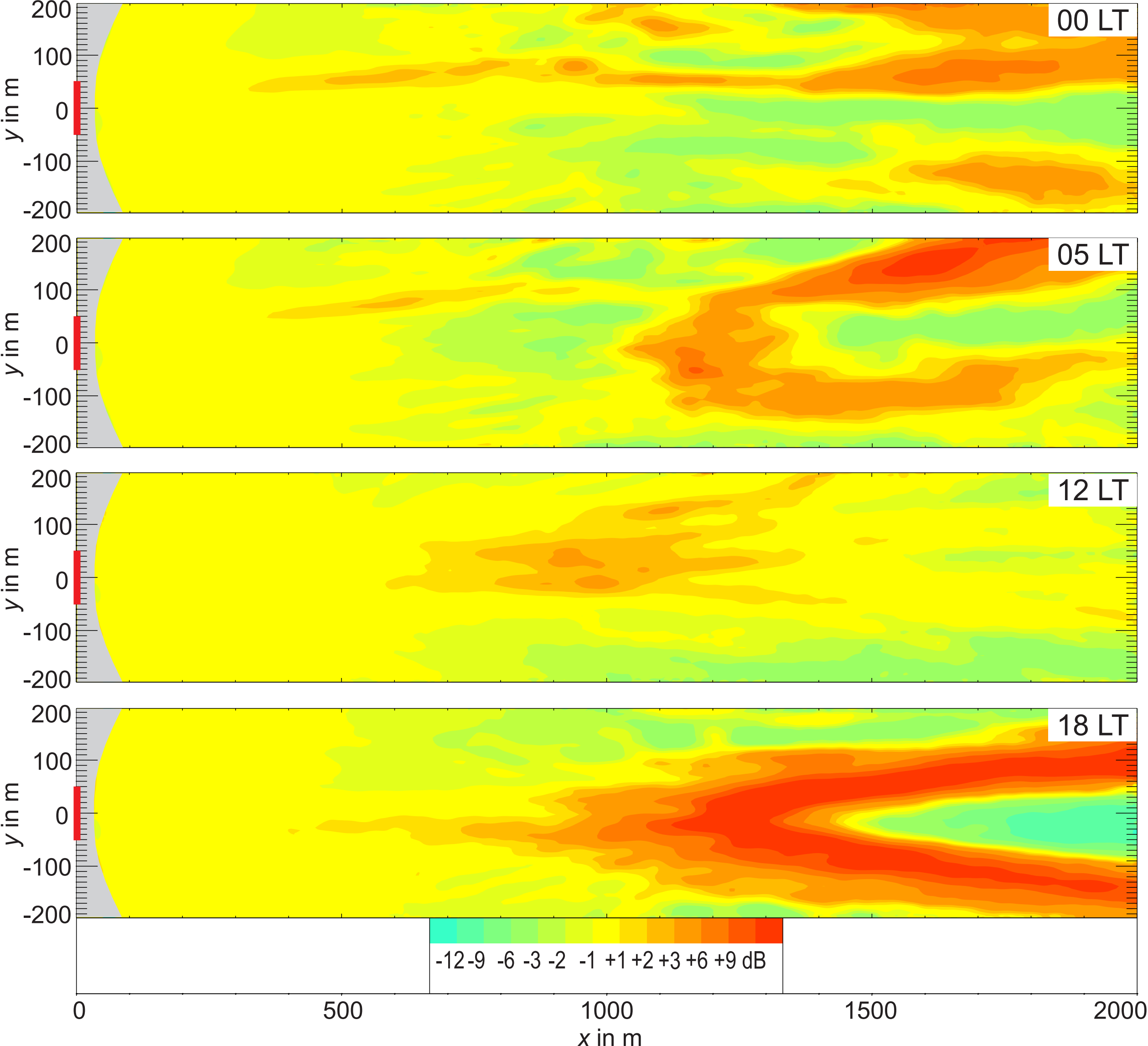

00 LT
05 LT
12 LT
18 LT
y in m
200
100
0
-100
-200
-12 -9 -6 -3 -2 -1 +1 +2 +3 +6 +9 dB
0
500
1000
1500
2000
x in m

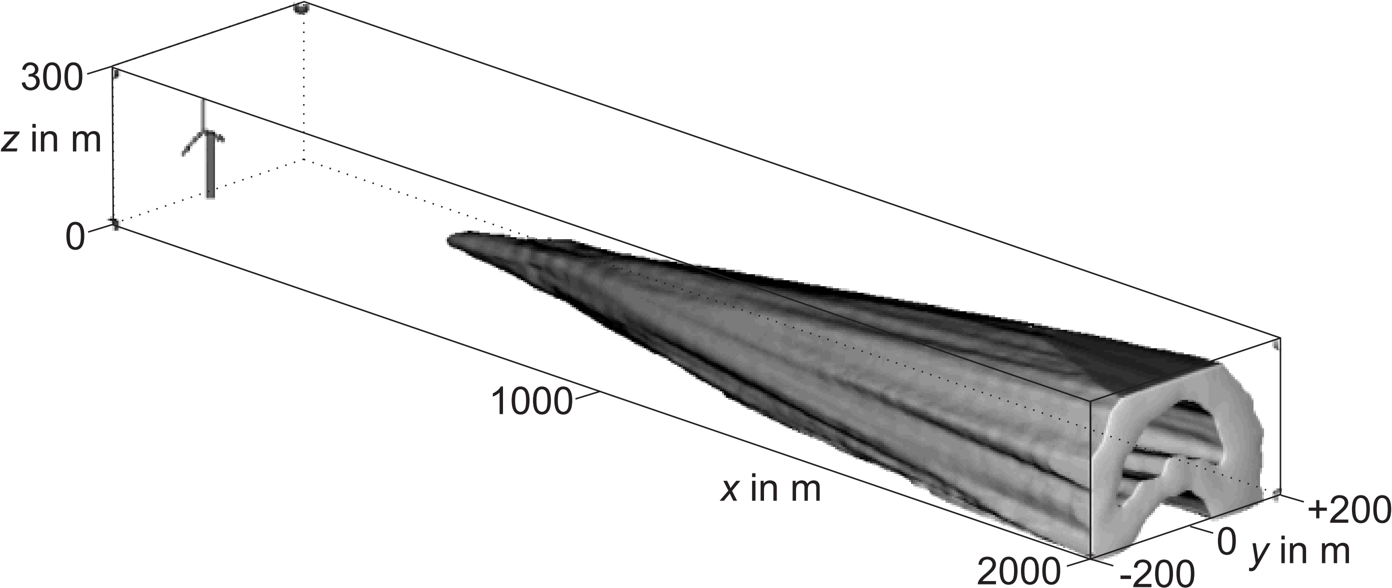

300
z in m
0
1000
x in m
2000
-200
0
+200
y in m

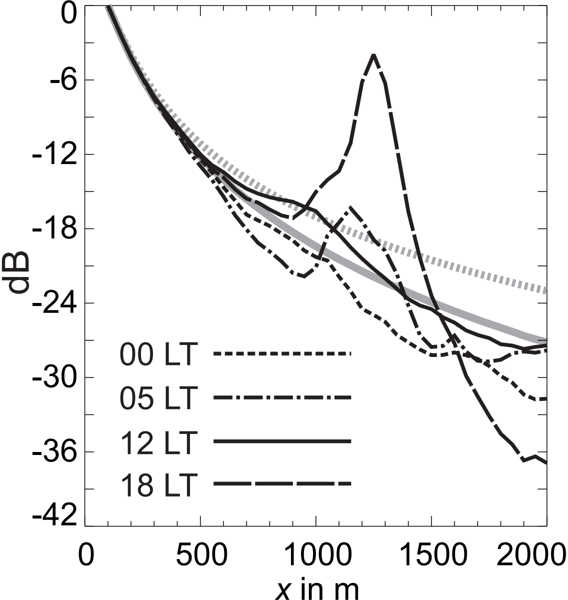

0
-6
-12
-18
-24
-30
-36
-42
dB
00 LT
05 LT
12 LT
18 LT
0
500
1000
1500
2000
x in m

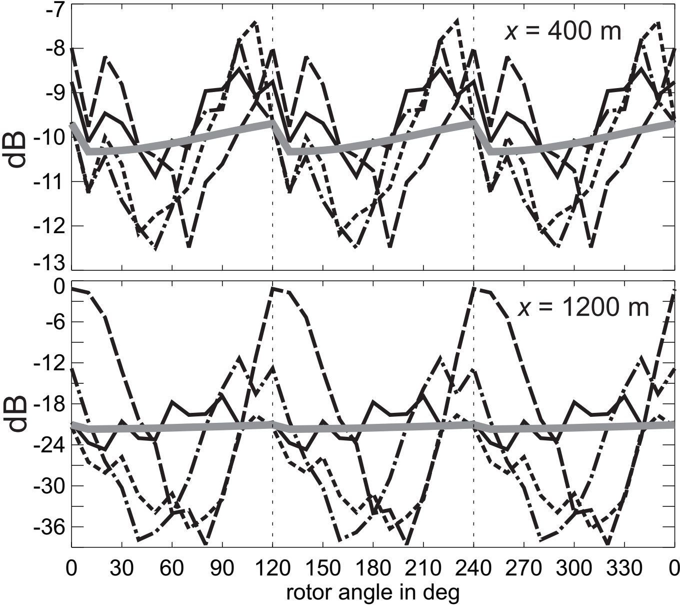

x = 400 m
dB
-7
-8
-9
-10
-11
-12
-13
x = 1200 m
dB
0
-6
-12
-18
-24
-30
-36
0 30 60 90 120 150 180 210 240 270 300 330 0
rotor angle in deg

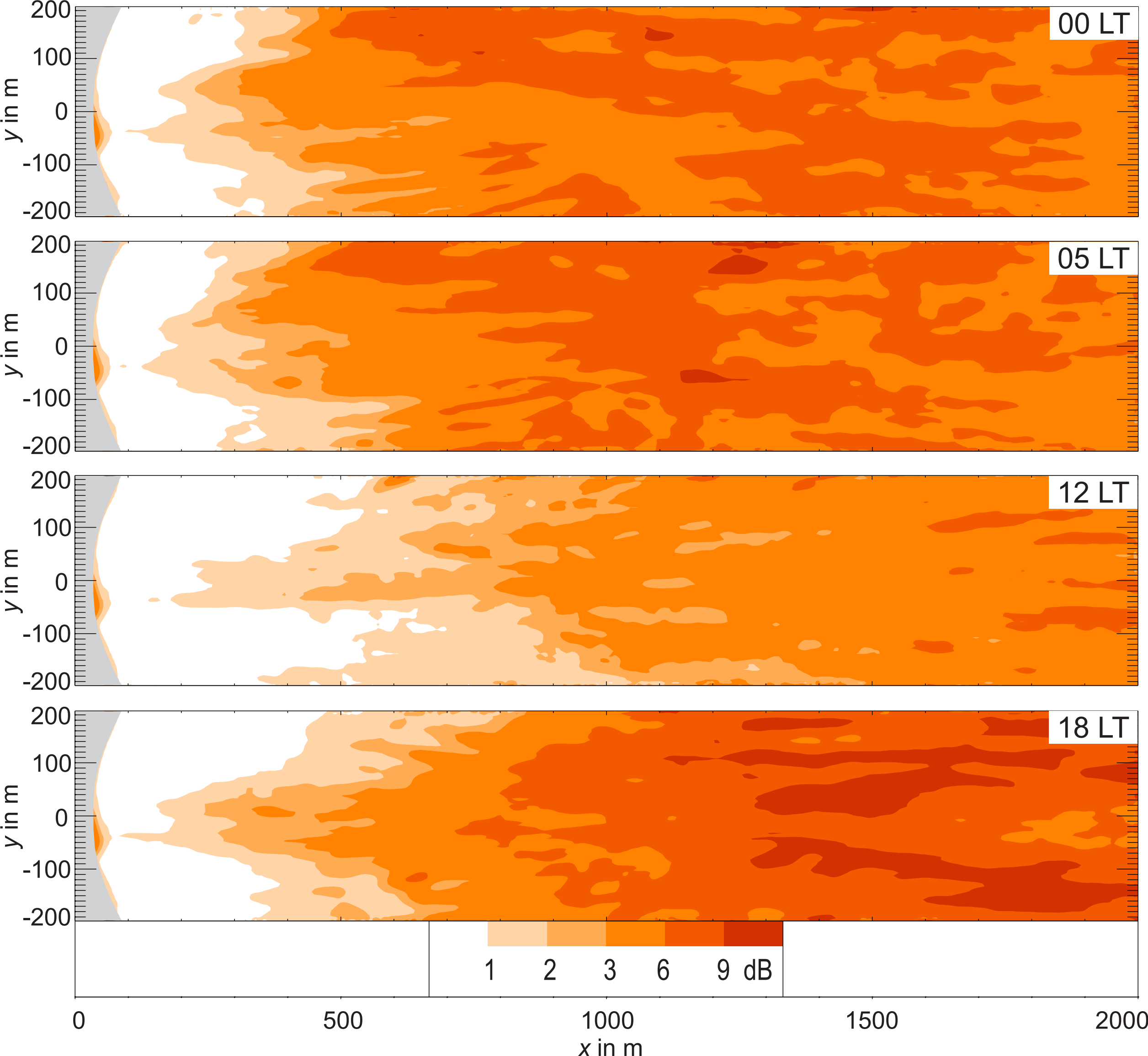

00 LT
05 LT
12 LT
18 LT
y in m
200
100
0
-100
-200
1
2
3
6
9
dB
0
500
1000
1500
2000
x in m